Electrostatic ion acceleration across a diverging magnetic field

D. Ichihara, A. Uchigashima, A. Iwakawa (iD), and A. Sasoh

View Online   Export Citation   CrossMark

ARTICLES YOU MAY BE INTERESTED IN

Effects of magnetic field profile near anode on ion acceleration characteristics of a diverging magnetic field electrostatic thruster
Journal of Applied Physics **122**, 043302 (2017); https://doi.org/10.1063/1.4995286

Electrostatic/magnetic ion acceleration through a slowly diverging magnetic nozzle between a ring anode and an on-axis hollow cathode
AIP Advances **7**, 065204 (2017); https://doi.org/10.1063/1.4985380

Electrostatic acceleration of helicon plasma using a cusped magnetic field
Applied Physics Letters **105**, 194101 (2014); https://doi.org/10.1063/1.4900423

Electrostatic ion acceleration across a diverging magnetic field

D. Ichihara,[a] A. Uchigashima, A. Iwakawa, and A. Sasoh

Department of Aerospace Engineering, Nagoya University, Nagoya, Aichi 464-8603, Japan

Electrostatic ion acceleration across a diverging magnetic field, which is generated by a solenoid coil, permanent magnets, and a yoke between an upstream ring anode and a downstream off-axis hollow cathode, is investigated. The cathode is set in an almost magnetic-field-free region surrounded by a cusp. Inside the ring anode, an insulating wall is set to form an annular slit through which the working gas is injected along the anode inner surface, so the ionization of the working gas is enhanced there. By supplying 1.0 Aeq of argon as working gas with a discharge voltage of 225 V, the ion beam energy reached about 60% of a discharge voltage. In spite of this unique combination of electrodes and magnetic field, a large electrical potential drop is formed almost in the axial direction, located slightly upstream of the magnetic-field-free region. The ion beam current almost equals the equivalent working gas flow rate. These ion acceleration characteristics are useful for electric propulsion in space. *Published by AIP Publishing.*
[http://dx.doi.org/10.1063/1.4960363]

Electric propulsion in space requires that ions be accelerated to an exhaust speed level that is not achievable by chemical propulsion. The typical energy level is in the order of 10^2 eV or higher.[1,2] For highly specific impulse propulsion, electrostatic acceleration methods such as ion thrusters[3] and Hall thrusters[4] are suitable because they accelerate only ions using a static electric field, without collisional dissipation processes. To obtain this effective acceleration, electrodes need to be carefully designed to avoid ion collisions as much as possible.[5] In ion thrusters, several grid electrodes are designed based on ion beam trajectory simulations.[6] In Hall thrusters, Mikellides *et al.* proposed the concept of "magnetic shielding" in which an acceleration channel design is combined with that for an applied magnetic field so that ion collisions against the discharge channel wall are mitigated with a superimposing magnetic field along the channel wall.[7] The efficiency of this scheme was demonstrated for 6-kW class laboratory Hall thrusters. However, the scheme is still under development, especially in a power range lower than 1 kW.[8] Cylindrical Hall thrusters,[9] high efficiency multistage plasma thrusters,[10] and cusped field thrusters[11] have a cusped magnetic field, so that the electric field is slightly inclined inward the radial direction in the effective ion acceleration region and the ion collisions with the wall are mitigated. Foster[12] demonstrated a wall-less ion acceleration using a cusped magnetic field. The anode is set at a cusp region and the cathode is set outside of it; thus, the main component of an accelerating electric field is almost parallel to the magnetic field. Under these electromagnetic fields, the xenon propellant utilization is almost 100%; however, for the argon propellant, it is less than 50%.[13]

Harada *et al.*[14] demonstrated the electrostatic acceleration of helicon plasma using a cusped magnetic field and electrodes (a ring anode and a hollow cathode) placed at the exit of the helicon plasma source (Helicon Electrostatic Thruster, HEST). The resulting ion beam had a higher energy than that of the double layer helicon thruster. Subsequently, Uchigashima *et al.*[15] demonstrated, with the same device as of Ref. 14, that under specific operating conditions, the inner surface of the ring anode is the main contributor to ion acceleration. As an essential difference from other thrusters, the electrostatic field between the anode and cathode goes across the diverging magnetic field. The electric field is somehow directed radially inward, and then the ion beam divergent angle is expected to be decreased, so that ion collision with the channel wall is mitigated. This electromagnetic field configuration make a completely another type of electrostatic thruster. By performing a thorough investigation of this device, we found that a helicon plasma source is not necessary to obtain ion acceleration. Furthermore, without the helicon plasma, ions are accelerated effectively under different operating conditions. In this study, we propose another type of electrostatic thruster and quantify the ion acceleration performance.

We named this device as "Diverging Magnetic field Electrostatic Thruster" (DM-EST). Figure 1 shows a schematic of the DM-EST examined in this study. The main components, such as the ring anode, magnetic circuit, and hollow cathode are the same ones as of Ref. 14. However, instead of the helicon plasma source, we included an insulating plate and an annular propellant injection slit at the ring anode entrance. The ring anode is made of copper with 27 mm of inner diameter and 10 mm of length and was placed 20-mm downstream from the solenoid coil center. The insulating wall was made of alumina and placed inside the ring anode. The insulating wall and the ring anode inner surface form an annular slit that is used to inject working gas along the ring anode inner surface.

Inside the ring anode, a diverging magnetic field with an angle of $1.3°$–$2.6°$ was applied. In the downstream region, the magnetic field generated by the solenoid coil was greatly modified using Nd-permanent magnets and a soft iron yoke. The hollow cathode (DLHC1000, Kaufman Robinson, Inc.)

[a]Author to whom correspondence should be addressed. Electronic mail: ichihara@fuji.nuae.nagoya-u.ac.jp.
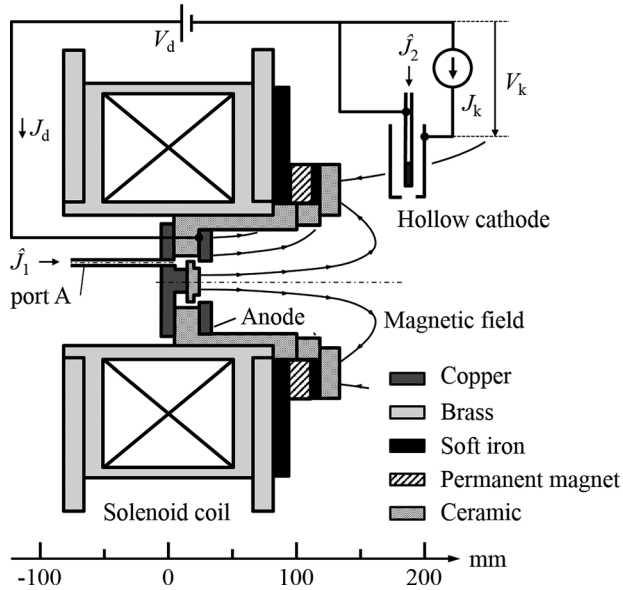
FIG. 1. Schematic of the DM-EST, side view.

orifice was placed 150-mm downstream from the coil center and 70-mm from the central axis.

As shown in Fig. 2, three different types of working gas injection ports (ports A–C) were tested. Port A (Fig. 2(a)) has a plug metal plate made of copper and an insulating wall with a projection diameter of 24 mm at the entrance of the ring anode. As mentioned above, this projection and the anode inner surface form an annular slit with a 2-mm length and a 1.5-mm width. The supplied working gas diffuses azimuthally in advance and flows inside the ring anode through the slit. Port B (Fig. 2(b)) has the same insulating wall geometry as of Port A, but with an additional 1.5-mm diameter

hole on the center axis. Only through this hole, the working gas is supplied inside the ring anode. Port C (Fig. 2(c)) does not have an insulating wall but is connected to a ceramic tube made of Photoveel with a 34-mm outer diameter and 27-mm inner diameter, which equals the ring anode inner diameter. The working gas of argon (purity 99.9999%) was supplied at each port (ampere equivalent flow rate of $\hat{J}_1$) and also through the hollow cathode ($\hat{J}_2$).

To measure the ion beam energy distribution function f in the exhaust plume, the same retarding potential analyzer (RPA)[16] as of Ref. 14 is used. The RPA was fixed at the center axis, 350-mm downstream from the anode entrance. To measure the ion beam current distribution $j_i(\theta)$, where the polar angle θ is measured from the accelerator center axis, the same Faraday cup as of Ref. 15 is swept in a longitudinal direction around the center axis of the thruster exit plane. Figure 3 shows an example of $j_i(\theta)$ that is normalized by $j_i(0)$. Assuming an axisymmetric ion beam distribution, the ion beam current J_i is estimated by

$$J_i = \int_{-\pi/2}^{\pi/2} j_i(\theta)\pi R^2 \sin\theta \, d\theta. \tag{1}$$

Here, R is the swing radius ($= 250\,\text{mm}$). $j_i(\theta)$ and the resulting J_i can be overestimated up to 10% due to a secondary electron emission from the copper collector surface.[17] Under the operating conditions in Fig. 3, J_i equals 1.21 A. Both $-\pi/2$ to 0 rad integration case with axisymmetric assumption and that of 0 to $\pi/2$ rad case were also evaluated. Resulting J_i changed against to Eq. (1) case by $+1.0\%$ in $-\pi/2$ to 0 rad integration case and -2.0% in 0 to $\pi/2$ rad case.

The electron number density n_e and electron temperature T_e are measured using a double probe. The space potential with respect to the cathode potential, V_s, is measured using a floating emissive probe. The double probe has two tungsten wires with 0.3 mm diameter and 5.0 mm length. The emissive probe has an emitting filament made of 1.0% thoriated tungsten wire with a diameter of 0.185 mm. The double or emissive probe was mounted on a stepping motor, and the survey time at each point is less than 0.2 s.
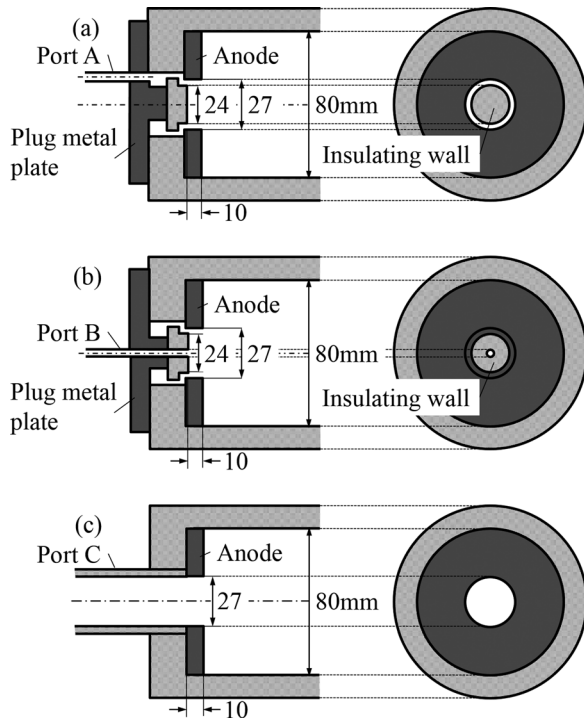

FIG. 2. Working gas injection ports: (a) port A, a single circular tube is connected to the cavity for introducing the gas to the annular slit, (b) port B, and (c) port C.
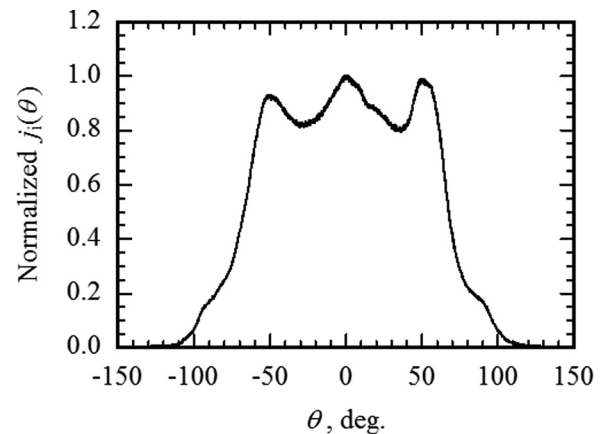

FIG. 3. Example of normalized ion beam current density j_i vs angle θ with respect to the accelerator center axis. The propellant gas was injected through port A. $\hat{J}_1 = 1.0$ Aeq, $\hat{J}_2 = 0.36$ Aeq, and $V_d = 200$ V.

The experiments are conducted in a 3.2-m long, 1.2-m diameter stainless steel vacuum chamber. The vacuum chamber is evacuated using a cryogenic pump with an exhaust speed of 8400 l/s, which is backed by a dry pump with an exhaust speed of 120 l/s. The ambient pressure, measured by an ionization gauge placed in the vacuum chamber wall at 590 mm upstream from the solenoid coil center, was maintained at 10 mPa with a total working gas flow rate $(\hat{J}_1 + \hat{J}_2)$ of 1.36 Aeq.

The hollow cathode is operated with $\hat{J}_2 = 0.36$ Aeq and a 2.0-A keeper current. $\hat{J}_1$ is fixed at 1.0 Aeq, and the discharge voltage V_d ranges from 150 to 250 V. In addition to J_i, the ion beam energy E_i and the discharge current J_d are measured at least twice in different operating conditions. The operating time was at least 3.5 s at each operating condition.

Figure 4 shows an example of f obtained by differentiation of the RPA signal with respect to V_{RPA} after normalizing J_c. Assuming that f is a linear combination of four different Gaussian functions, the rough J_c is smoothly fit and the parameters of each Gaussian function are estimated using the least squares method. In Fig. 4, f has two peaks: at $V_{RPA} = \varphi_1 (= 35 \text{ V})$ and at $V_{RPA} = \varphi_2 (= 151 \text{ V})$. Here, φ_1 equals a space potential at the RPA position and φ_2 is the ion beam energy with respect to the cathode potential. Using the variances of each Gaussian function corresponding to each peak, E_i and its standard deviation are defined by

$$E_i = \varphi_2 - \varphi_1 \pm \sqrt{\sigma_1^2 + \sigma_2^2}. \qquad (2)$$

Thus, in the case shown in Fig. 4, we have $E_i = 116 \pm 29$ eV.

Figure 5 shows the ion beam and discharge characteristics with different working gas injection ports. The averaged values are shown as symbols and the standard deviation defined in Eq. (2) as error bars. Using port A, E_i increases almost linearly with V_d with a rate of $dE_i/dV_d = 0.65$. J_i almost saturates to the value equivalent to the total working gas flow rate, $\hat{J}_1 + \hat{J}_2$. At $V_d = 225$ V, J_i reaches 96% of $\hat{J}_1 + \hat{J}_2$, which is much higher than the values obtained using the other injection ports. Under this operating condition, $J_d = 2.1$ A, which is larger than $\hat{J}_1$ by a factor of about 2.

Figure 6 shows an example of the n_e, T_e, and V_s distributions with port A. The coordinates r (radial) and z (axial)

FIG. 5. V_d vs. E_i, J_i, and J_d with varying working gas injection ports. $\hat{J}_1 = 1.0$ Aeq, and $\hat{J}_2 = 0.36$ Aeq.

have the origin at the left-hand surface of the ring anode on the center axis. As shown in Fig. 6(a), electrons are radially confined around the center axis by the diverging magnetic field. n_e has a peak value of $3.2 \times 10^{18}\,\text{m}^{-3}$ in the vicinity of the anode inner surface. This ionization enhancement is known as the "hollow-anode effect"[12,18] by which the injected cold gas is efficiently ionized near the anode. At this position, V_s was 170 V, which is lower than the anode voltage by 30 V. This voltage drop is higher than the ionization energy of argon (15.8 eV) and some portion of the working gas is ionized by collisions with the accelerated electrons through this voltage drop.

The location where T_e has a maximum (higher than 30 eV) is shifted downstream at $z = 90–110$ mm (see Fig. 6(b)), as
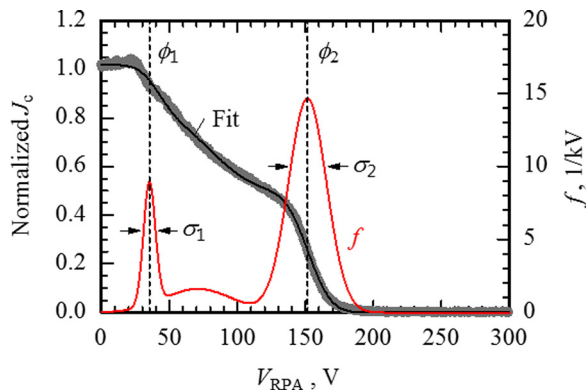

FIG. 4. Example of the normalized ion current J_c and the corresponding ion energy distribution function f. The propellant gas was injected through port A. $\hat{J}_1 = 1.0$ Aeq, $\hat{J}_2 = 0.36$ Aeq, and $V_d = 200$ V.
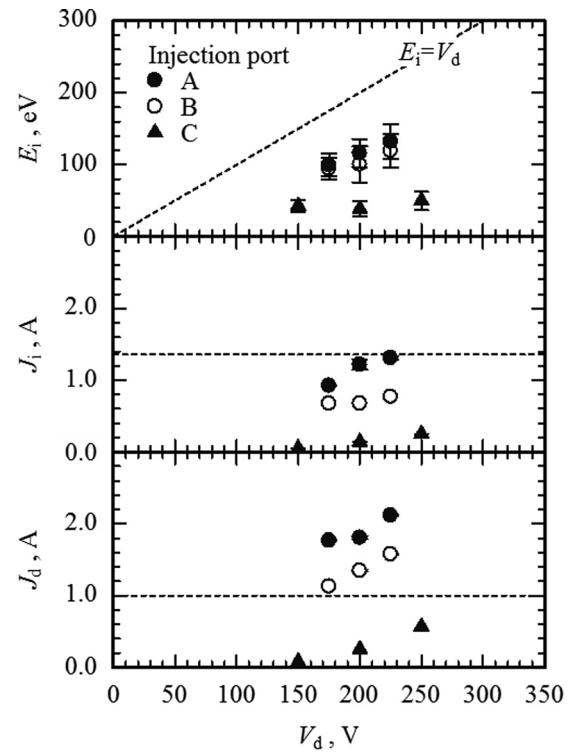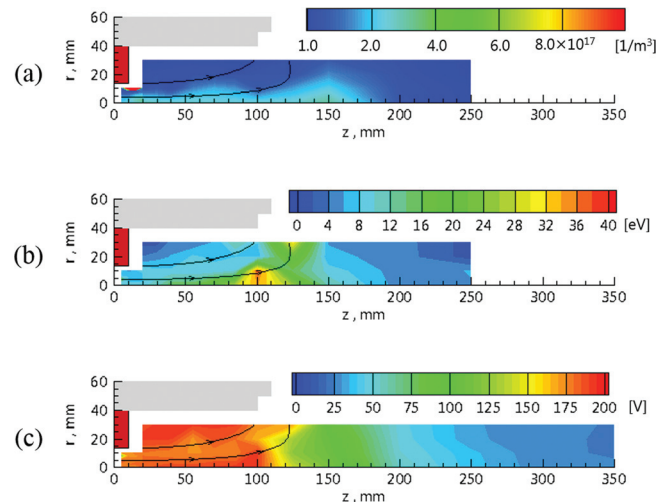

FIG. 6. n_e, T_e, and V_s distributions using port A in $\hat{J}_1 = 0.50$ Aeq, $\hat{J}_2 = 0.36$ Aeq, and $V_d = 300$ V operating conditions. (a) n_e, 1/m^3, (b) T_e, eV, and (c) V_s, V.

the magnetic field rapidly diverges in the magnetic-field-free region. Immediately downstream from this zone, V_s starts decreasing toward downstream by 150–160 V in the region of the measurement. Therefore, the whole scenario of ion's generation and acceleration is as follows: At the entrance slit in the anode's inner surface, the introduced neutral gas is ionized by electrons that gain a kinetic energy by the radial potential difference of the order of 30 V. Then, the ions are accelerated mainly in the axial direction at the exit of the diverging magnetic nozzle. This ion acceleration scenario is favorable for avoiding ion beam collisions against the acceleration channel wall.

By injecting the working gas through port B, E_i, J_i, and J_d are decreased by at most 14%, 45%, and 37% of port A, respectively. Using port B, the working gas was not efficiently ionized because such radial potential drop could not be formed near the anode's inner surface. When the working gas is injected through port C, E_i remains at low values of 38–49 eV, 38%–45% of the ones obtained in port B. J_i and J_d also remain at a lower level. The only difference between ports B and C is the presence of the insulating wall. At $V_d = 200$ V, J_i and J_d are, respectively, 20% and 18% of port B. Further investigation is necessary for a quantitative understanding of the mechanisms that involve the insulating wall.

In this study, we experimentally demonstrated electrostatic ion acceleration across a diverging magnetic field using a ring anode with an insulating wall and an off-axis hollow cathode. By injecting argon as working gas along the inner surface of the ring anode, the ionization was efficiently done by the hollow-anode effect, and the ions were accelerated to a beam energy equivalent to about 60% of a discharge voltage. From plasma diagnostics using double and emissive probes, an efficient ionization near the anode inner wall and an axial potential drop near the exit of the diverging magnetic field were demonstrated. The evaluation of thruster performance from three-dimensional probe surveys, direct thrust measurements, and better understanding of the ion acceleration mechanisms deserve further investigations.

[1]D. M. Goebel and I. Katz, *Fundamentals of Electric Propulsion: Ion and Hall Thrusters* (John Wiley & Sons, 2008), pp. 429–446.

[2]D. Y. Oh, J. S. Snyder, D. M. Goebel, R. R. Hofer, and T. M. Randolph, "Solar electric propulsion for Discovery-class missions," J. Spacecraft Rockets **51**, 1822–1835 (2014).

[3]J. Snyder, D. M. Goebel, R. R. Hofer, J. E. Polk, N. C. Wallace, and H. Simpson, "Performance evaluation of the T6 ion engine," J. Propul. Power **28**, 371–379 (2012).

[4]A. I. Morozov and V. V. Savelyev, *Fundamentals of Stationary Plasma Thruster Theory* (Springer, New York, 2000), pp. 203–391.

[5]M. Keidar, I. D. Boyd, and I. I. Beilis, "Plasma flow and plasma–wall transition in Hall thruster channel," Phys. Plasmas **8**, 5315–5322 (2001).

[6]C. C. Farnell and J. D. Williams, "Ion thruster grid design using an evolutionary algorithm," J. Propul. Power **26**, 125–129 (2010).

[7]I. G. Mikellides, I. Katz, R. R. Hofer, and D. M. Goebel, "Magnetic shielding of a laboratory Hall thruster. I. Theory and validation," J. Appl. Phys. **115**, 043303 (2014).

[8]R. W. Conversano, Ph.D. thesis, University of California, Los Angeles, 2015.

[9]K. D. Diamant, J. E. Pollard, Y. Raitses, and N. J. Fisch, "Ionization, plume properties, and performance of cylindrical Hall thrusters," IEEE Trans. Plasma Sci. **38**, 1052–1057 (2010).

[10]N. Koch, H. P. Harmann, and G. Kornfeld, "Development and test status of the THALES high efficiency multistage plasma (HEMP) thruster family," in *Proceedings of the 29th International Electric Propulsion Conference*, Princeton, USA (2005), IEPC Paper No. 2005-297.

[11]N. A. MacDonald, C. V. Young, M. A. Cappelli, and W. A. Hargus, Jr., "Ion velocity and plasma potential measurements of a cylindrical cusped field thruster," J. Appl. Phys. **111**, 093303 (2012).

[12]J. E. Foster, "Compact plasma accelerator device," Rev. Sci. Instrum. **73**, 2020–2027 (2002).

[13]A. Shabshelowitz and A. D. Gallimore, "Performance of a helicon hall thruster operating with xenon, argon and nitrogen," J. Propul. Power **30**, 664–671 (2014).

[14]S. Harada, T. Baba, A. Uchigashima, S. Yokota, A. Iwakawa, A. Sasoh, T. Yamazaki, and H. Shimizu, "Electrostatic acceleration of helicon plasma using a cusped magnetic field," Appl. Phys. Lett. **105**, 194101 (2014).

[15]A. Uchigashima, T. Baba, D. Ichihara, A. Iwakawa, A. Sasoh, T. Yamazaki, S. Harada, M. Sasahara, and T. Iwasaki, "Anode geometry effects on ion beam energy performance in helicon electrostatic thruster," IEEE. Trans. Plasma Sci. **44**, 306–313 (2016).

[16]J. A. Simpson, "Design of retarding field energy analyzers," Rev. Sci. Instrum. **32**, 1283–1293 (1961).

[17]M. A. Lieberman and A. J. Lichtenberg, *Principles of Plasma Discharges and Material Processing*, 2nd ed. (John Wiley & Sons, Inc., 2010), p. 302.

[18]A. Anders and S. Anders, "The working principle of the hollow-anode plasma source," Plasma Source Sci. Technol. **4**, 571–575 (1995).